ChemElectroChem

Research Article
doi.org/10.1002/celc.202400506

Chemistry Europe
European Chemical Societies Publishing

www.chemelectrochem.org

Advancing Bipolar Electrochemistry for Targeted Deposition of Biocompatible Polymers in Electrolyte-Free Solutions *via* Finite Element Modeling

Michal Wagner,*[a] Áine Brady,[a] Oisín F. Doyle,[a] and Robert J. Forster*[a, b]

The spatially controlled, template-free, deposition of electroactive and biocompatible materials on 3D objects is of great interest for wireless cell stimulation intended for diverse applications ranging from electroceuticals to advanced sensor development. Bipolar electrochemistry provides the possibility of depositing electrically conducting polymers controlled through the (shaped) electric field distribution. A second advantage is that electrochemistry can be performed in electrolyte-free media potentially removing the "interfering" effect of added electrolyte. Here, poly(3,4-ethylenedioxythiophene) (PEDOT) films have been deposited on bipolar electrodes directly in ultrapure water. Significantly, the deposition patterns cannot be fully explained using a linear change in the solution-phase potential, which is a common assumption for bipolar electrochemical systems. 3D finite element modeling and diffusive mass transport considerations have been combined to map the electric field distribution in this very low conductivity medium and demonstrate that homogenous rather than heterogeneous electron transfer is likely to play an important role in polymer deposition. Moreover, modeling predictions were compared to electrochemical impedance and cyclic voltammetry results and non-linear behaviours qualitatively matched, through film capacitances, and deposition patterns. The proposed framework opens up significant opportunities for the template-free deposition of various electroactive materials on bipolar electrodes in low-conductivity solutions.

Introduction

Electrical stimulation of biological cells is an ever-increasing approach in applied medicine[1] and mechanistic studies,[2] since it can effectively influence the intracellular environment and signal transduction pathways[3] in a non-destructive manner. Electrostimulation devices can greatly benefit from implementing wireless approaches where no physical contact is needed between stimulus electrodes and driver circuits, thus further extending their adaptability for specific *in vivo* applications. Among prospective approaches, bipolar electrochemistry offers a versatile framework for minimally invasive, cost-effective, and adaptable biological cell stimulation.[4] Bipolar electrochemical systems typically consist of two working 'feeder' electrodes (FEs) immersed in the desired medium and spaced with the third 'floating' bipolar electrode (BPE).[5] The latter electrode is subjected to polarization without direct electronic contact *via* an electric field generated by FEs. In biological studies, it is preferential to interface cell cultures and BPE with biocompatible materials while the electroactivity of the interlayer is preserved. Electrically conducting polymers are a group of materials that can provide this dual function.[6] Moreover, electronic and ion-to-electron transduction properties of conducting polymers can be altered to enhance electrochemical "communication" between cells and BPE.[7] Conducting polymers such as sulfonated polyaniline along with more common polypyrrole and poly(3,4-ethylenedioxythiophene) (PEDOT) are extensively applied in biomedical settings.[8,9] Importantly, listed here polymers can readily be made by anodic electropolymerization, thus opening possibilities for deposition on various conducting 2D and 3D objects whose shape can trigger certain cell culture responses such as proliferation, adhesion, and differentiation.[10]

Since the electric field distribution is mainly controlled by the geometry of the system,[11] the electrochemical deposition of conducting polymers can be confined to a specific region of BPE. For planar BPE centered midway between FEs, the electric field distribution typically results in a gradual change in solution overpotentials along the surface of BPE, with anodic and cathodic polarization of opposing BPE sides.[11] Therefore, anodic polymerization of conducting polymers in such a system results in asymmetric deposition patterns and regions of preferential deposition. Exemplary controlled patterning of conducting polymers with submillimeter precision *via* bipolar electrochemistry has been achieved,[12] as well as the fabrication of conducting polymer wires driven by dendritic growth in bipolar systems,[13,14] all being promising for bioelectronic applications. In order to gain control over the asymmetric

[a] *Dr. M. Wagner, Dr. Á. Brady, O. F. Doyle, Prof. R. J. Forster*
School of Chemical Sciences
Dublin City University, Dublin 9, Ireland
E-mail: michal.wagner83@gmail.com
robert.forster@dcu.ie

[b] *Prof. R. J. Forster*
FutureNeuro, SFI Research Centre for Chronic and Rare Neurological Diseases
Dublin City University, Dublin 9, Ireland

Supporting information for this article is available on the WWW under https://doi.org/10.1002/celc.202400506

deposition of conducting polymers, *i.e.*, to ultimately develop a template-free approach to the spatially controlled electrodeposition, (I) mass transport and interfacial kinetics, as well as (II) the relation of the BPE system geometry with electric field theory, need to be well understood. Significant efforts have been undertaken toward modeling the electrode-electrolyte solution interface in bipolar electrochemical systems, such as faradaic (de)polarization,[15,16] charging-discharging dynamics and kinetics,[17,18] as well as generalized algorithms for solving potential and current distributions.[19] Importantly, the local distribution of various electrochemical quantities can be modeled with the finite element method (FEM).[20] This technique was successfully applied to map potential distributions in proximity to BPE surfaces and confirmed by experimental potential measurements.[21,22] However, these investigations have been focused on electrochemical systems with relatively high ionic strengths where ions are freely available.

In this work, we explore the electrochemical synthesis and deposition of the PEDOT process in bipolar systems in the absence of deliberately added electrolyte, *i.e.*, where the solution only contains ultrapure water and the monomer. This strategy seeks to address one of the main disadvantages of electrochemistry compared to spectroscopy, *i.e.*, that the sample must be "contaminated" with supporting electrolyte. Specifically, in the case of the deposition of conducting polymers, it opens up the possibility of creating novel underdoped materials and could provide deep insights into the relative importance of ionic *vs.* electronic conductivity in these systems. Moreover, for wirefree electroceuticals purely aqueous, electrolyte-free media can minimize aggregation of proteins,[23] as well as kosmo- and chaotropic effects.[24] Encapsulation of function-specific proteins in conducting polymer matrix is highly attractive for understanding and controlling electrochemical communication with biological cells. Thus, a thorough understanding of the potential distribution and the factors that control the synthesis and deposition of electroactive materials in high-resistance solutions is needed. Ultralow ion concentrations are expected to significantly influence the potential distribution at the electrode-solution interface.[25] Therefore, we conducted a systematic 3D FEM modeling of both potential and potential gradient distributions in bipolar systems and subsequently estimated limitations for diffusive mass transport important for experimental PEDOT deposition on BPEs in ultrapure water. The experimentally observed PEDOT film deposition patterns are in excellent qualitative agreement with the modeling predictions and cannot be fully explained using conventional approaches describing bipolar electrochemistry in the presence of electrolyte. We believe that our modeling approach represents a significant opportunity to *a priori* predict the complex potential distributions that can occur in bipolar systems allowing, for example, different regions of a 3D cell culture array to receive different electrical, electrochemical and chemical stimuli simultaneously.

Methods

Modeling

Three different lengths (1.4, 2, and 2.6 cm) of BPE samples were chosen for FEM simulations, referred to in this work as **1.4 cm BPE**, **2 cm BPE**, and **2.6 cm BPE**, respectively. Each BPE is 1 cm in width and 0.23 cm in height consisting of a glass slide coated with a 550 nm thick fluorine-doped tin oxide (FTO) layer, Figure 1. In the model, the FTO-coated glass BPEs are placed between two titanium FEs (WE1 and WE2) spaced by 3 cm and with the following dimensions: length = 0.2 cm, width = 1.2 cm, and height = 2 cm. The electrical conductivities (σ) of FEs,[26] the medium, glass body,[27] and FTO are set to 2.38×10^{6}, 5.5×10^{-6}, 1×10^{-11}, and 2.6×10^{5} S m^{-1}, respectively. Significantly, these values reflect the very large differences in conductivity of the electrodes compared to the medium which has profound implications for the potential distribution and current flow pathways. Both BPEs and FEs were placed within a continuous medium (length = 9.4 cm, width = 7.2 cm, height = 8 cm) whose outer surfaces represent a Dirichlet boundary of 0 V. The same boundary type was applied to the surfaces of FEs which were 'electrified' by $\pm$5, 10, 15, and 20 V, in order to create the desired electric field ($\vec{E}$) in the studied systems. Additionally, the system where the BPE is absent is referred to as **0 cm BPE** and was also analyzed with the same set of potentials to gain insights into the impact of the presence of the BPE on potential and electric field distributions. The BPEs are positioned with a central axis located at the interface between the FTO layer and the medium. 3D models were built using FreeCAD 0.21.1 and meshed in Salomé 9.12.0 with 'NETGEN 1D-2D-3D' algorithm. For all FEM simulations, Elmer solver[28] was used and data were visualized using ParaView 5.11.2 software. The electric potential (φ) and the modulus of potential gradient ($|\phi| = \nabla\varphi$) were calculated utilizing Elmer's static current conduction and flux computation modules, through the following Poisson's equation describing the total charge density (ρ_t) based on the

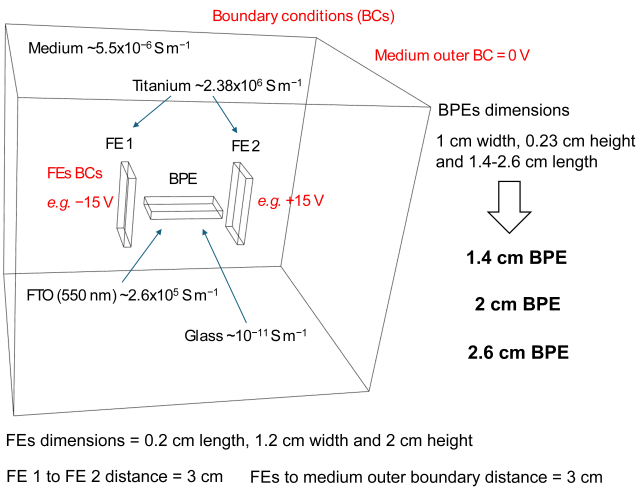

Figure 1. The schematic of studied BPE systems used for FEM simulations.

electric field relationships with current density ($\vec{J} = \sigma\vec{E}$) and potential gradient ($\vec{E} = -\nabla\varphi$):

$$-\nabla \cdot \sigma\nabla\varphi = \rho_t \quad (1)$$

Empirical Verification

FTO glass slides with 550 nm coating having a sheet resistance of ~7 Ω sq^{-1} were obtained from Sigma-Aldrich and cut into dimensions equivalent to **1.4 cm BPE**, **2 cm BPE**, and **2.6 cm BPE** modeled samples. Before polymer deposition, the samples were ultrasonicated in isopropyl alcohol for 10 min and dried with nitrogen gas. The chemicals 3,4-ethylenedioxythiophene (EDOT, 97%) and lithium perchlorate (≥95%) were obtained from Sigma-Aldrich and used as received. All aqueous solutions were prepared with freshly deionized water (18.2 MΩcm resistivity) obtained with the Mili-Q ultrapure water system. For electrochemical polymerization of PEDOT *via* the bipolar approach, two polished titanium feeder electrodes, FEs, with dimensions similar to modeled electrodes were inserted into in-house 3D printed cells made of acrylonitrile butadiene styrene. The Ti FEs were separated by 3 cm and BPE samples were placed midway between the two FEs marking the center of the bipolar system. In each 10-minute deposition run, 3 mL of 10 mM EDOT (aq) was used, and potential difference ($\triangle\varphi_{app}$) of 10, 20, 30, and 40 V were applied across the FEs using DC laboratory power supply (max. 200 V, EA-PS 5200-02A, Elektro-Automatik). After deposition, PEDOT films were rinsed with ultrapure water to remove any residual monomer and left to dry at ambient conditions. Subsequently, the PEDOT/FTO samples acted as working electrodes (WEs) in conventional 3-electrode cells for cyclic voltammetry (CV) and electrochemical impedance spectroscopy (EIS) experiments (utilizing Metrohm Autolab PGSTAT204 potentiostat/galvanostat controlled by Nova 2.1 software). These measurements were carried out in 0.1 M $LiClO_4$ (aq) to obtain film capacitance (C_f) and Warburg admittance (Y_0) values. WEs were masked using Teflon tape so that a 1 cm^2 area was analyzed (*vide* Figure S1c). A platinum wire coil and a Ag/AgCl (1 M KCl) acted as counter electrode (CE) and reference electrode (RE), respectively. All samples were cycled from −0.1 to +0.5 V at 5, 10, 20, 50, and 100 mV s^{-1} scan rates, *i.e.*, they were doped with perchlorate anions. Before and after CV studies, potentiostatic EIS measurements were conducted within the 100k–0.1 Hz frequency range (61 data points per one measurement) at 10 mV excitation amplitude and a fixed potential of 0.2 V. The latter potential was selected for C_f estimations for both CV and EIS since it represents a clear current plateau region where the PEDOT film response is dominated by capacitance (*vide* Figure S1a). In the case of EIS, obtained impedance spectra were fitted to the following equation (Randles circuit in series with C_f):

$$Z(\omega) = R_S + \left(j\omega C_{dl} + \frac{1}{R_{ct} + W_c(1-j)/\sqrt{\omega}}\right)^{-1} + \frac{1}{j\omega C_f} \quad (2)$$

where, ω is angular frequency, R_S is solution resistance, C_{dl} is double-layer capacitance, R_{ct} is charge transfer resistance, and Y_0 ($1/W_C$) is the magnitude of admittance (in S $s^{0.5}$) of the Warburg element. For C_f estimation from CV, both anodic and cathodic currents were considered and plotted against the applied scan rate values, followed by linear regression to obtain slopes of the fitting lines (*i.e.* C_f). Triplicates for PEDOT deposition on each BPE (1.4, 2, and 2.6 cm) were independently fabricated and subjected to CV and EIS analysis. All experiments were performed at room temperature (21.5 ± 1.5 °C).

Results and Discussion

First, the experimental deposition of PEDOT using bipolar electrochemistry in the absence of deliberately added electrolyte is considered. In the conventional model, the potential induced in the BPE by the electric field is expected to decay linearly across electrode length. This distribution gives the largest potential at the BPE edges closest to the FEs and the linear decay would be expected to give a film thickness that decreases uniformly towards the center of the BPE if electrodeposition is controlled by overpotential dependent heterogeneous electron transfer, resulting in "wedge" shape films. Figure 2a shows that the wireless electrodeposition of PEDOT on FTO glass BPEs in ultrapure water was successful for all the applied voltages and selected electrode lengths. The presence of PEDOT films was confirmed by comparative CV and EIS experiments with PEDOT made in a standard 3-electrode system (*vide* Figure S1). As can be seen from Figure 2a some aspects predicted by the linear decay model are present, *e.g.*, the film is thickest at the edges and becomes thinner towards the center of the BPE. However, the film is significantly more structured than expected, since preferential deposition occurs at all the edges within the anodic region of BPE. Similar intensity distribution maps were obtained *via* electrochemiluminescence (ECL) imaging of luminol in bipolar systems,[29] while more uniform patterns were observed for fluorescence monitoring of "microfluidic" BPEs at very high field strengths (around 200 kV m^{-1}).[30] However, optical assessments alone are not sufficient for the characterization of the material deposition process.

Importantly, electrodeposited PEDOT films on BPEs were subjected to both CV and EIS techniques to obtain C_f values which is a useful measure of the quantity of PEDOT deposited. Capacitance values were obtained by calculating slopes of the fitting lines for both anodic and cathodic currents *vs.* applied scan rate, as well as applying the Randles-based equivalent circuit model (*vide* Equation 2) to impedance spectra. The summary of this analysis is presented in Figure S2, while refined C_f *vs.* $\triangle\varphi_{app}$ plots are shown in Figure 2b. The capacitance is expected to increase proportionally to the amount of the material deposited which, if potential-dependent heterogeneous electron transfer is rate determining step, should depend on the voltage applied to FEs. However, for the **1.4 cm BPE** sample, the obtained profile does not follow the expected linear dependence, while the **2 cm BPE** and **2.6 cm BPE** samples exhibit unexpectedly similar capacitance characteristics. Addi-

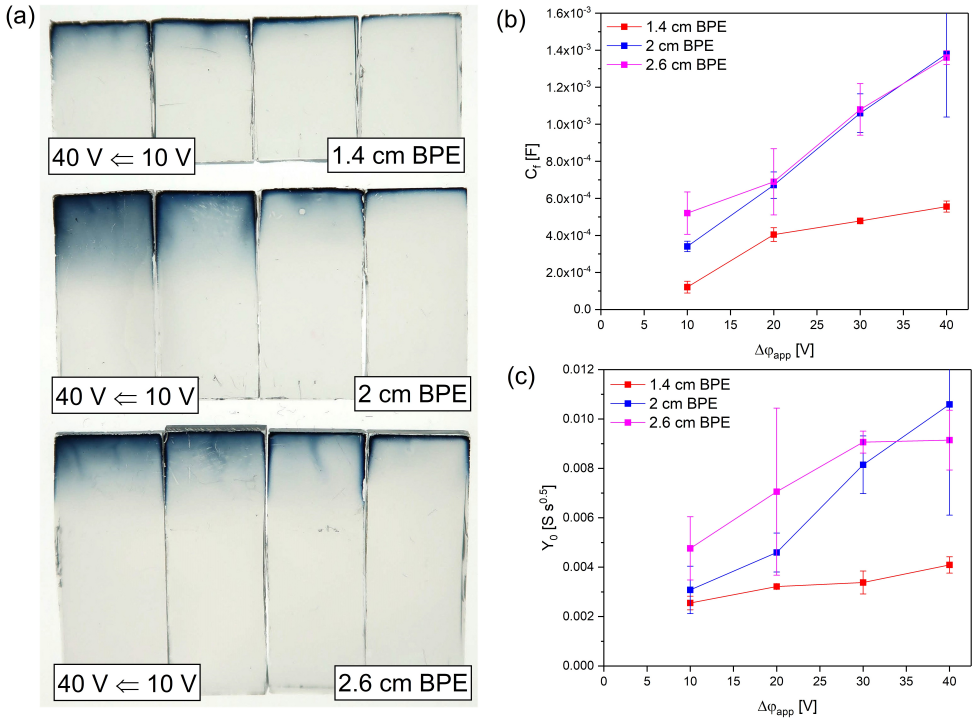

Figure 2. Photographs of exemplary PEDOT samples deposited on FTO glass (a). Estimated PEDOT film capacitance (C_f) values from CV (b) and admittance (Y_0) from Equation 2 (c) as a function of applied voltage (3 replicas).

tionally, the approximation of the general trends in mass diffusivity in the studied PEDOT films can be derived from the analysis of the magnitude of admittance (Y_0) characteristic for the Warburg element, Figure 2c. For an electrochemical system, this electrical quantity can be related to the diffusional time constant and thus to the diffusion coefficient.[31] Since the deposition of PEDOT on BPEs results in films with significant thickness inhomogeneity, the Y_0 values represent average quantities across the film. The Y_0 *vs.* $\triangle\varphi_{app}$ profiles for **2 cm BPE** and **2.6 cm BPE** samples exhibit relatively high levels of non-linearity and are similar to capacitance profiles shown in Figure 2b when taking into account variability in the dataset.

In the frequently used approximation of polarization of conducting BPE due to applied voltage ($\triangle\varphi_{app}$),[5,11] the magnitude of the combined solution overpotentials (anodic and cathodic, $\triangle\varphi_{BPE}$) changes linearly with $\triangle\varphi_{app}$ according to the proportionality factor in the form of BPE length/cell length ratio. The floating potential of BPE (φ_{BPE}) reside within $\triangle\varphi_{BPE}$ bounds and reflect the equilibrium state. On the other hand, at a microscopic level, the effective capacitance of the Stern layer plays a significant role in the potential and charge distributions at the BPE-solution interface.[17] The potential drop across the Stern layer at the reaction plane is connected with local electric field strength.[32,33] Therefore, for a reaction to occur *via* electron tunneling, the interfacial potential difference between BPE and solution ($\varphi_{BPE} - \varphi$) needs to be adequately significant in the proximity of the Stern layer. The kinetics of a reaction can be then described within the Frumkin–Butler–Volmer theory[34] and the resultant Faradaic current linked with local surface charge dependent on both Stern layer thickness and $\varphi_{BPE} - \varphi$ magnitude. For the electrochemical deposition of PEDOT on BPE in ultrapure water very large Debye lengths are expected (>30 nm). Hence, the surface charge density and resultant polarization of BPE seem to be not sufficient for electron transfer to occur directly at the BPE/solution interface. Moreover, the significant drop of around 1 V (for $\triangle\varphi_{app} = 10$ V) in solution potential near BPE edges measured above 100 and 300 μm corroding stainless steel surface[22] suggests rather low solution potential values at the length scale of the electric double layer.

It is therefore apparent that a theoretical analysis of induced electric fields in bipolar electrochemical systems with significant differences in conductivity between the BPE material and the surrounding solution phase is required. Multiphysics simulations of electrodynamics on 3D objects can be performed utilizing the FEM technique addressing geometry/boundary constraints and material conductivities. Overall, four 3D models of bipolar systems were built representing **1.4 cm BPE**, **2 cm BPE**, and **2.6 cm BPE** samples including a "reference" system where no BPE is present, referred to as **0 cm BPE**. In the model schematic presented in Figure 1, both FEs were equidistant to the outer boundary by 3 cm. This choice of geometry enabled the unimpeded development of the electric field in the opposite direction to the BPE, since the focus of the work was to study and quantify the interaction of BPE with FEs and thus resultant PEDOT film formation mechanism without the interference of other structural components. Moreover, the potential on the outer boundary was fixed at 0 V to provide conditions

resembling electric continuity extending to infinity. Since the total charge density is proportional to the potential gradient *via* the electric conductivity of a specific medium (*vide* Equation 1), the distribution of electrical quantities is clearly governed by the composition and geometry of both the model and actual BPE systems.

Typical φ and |∇φ| distributions within both the medium and BPE are shown in Figure 3b. The presence of the BPE results in significant changes in the potential distribution associated with the non-zero gradual asymmetric distribution of electric field within the underlying glass and near the surface of FTO, Figure S3. The FTO is only approximately one order of magnitude less conducting than the Ti FEs, therefore effectively no net electric field is expected within the FTO layer. This results in $\varphi = 0$ (in respect to infinity) directly along the FTO/medium interface in contrast to non-zero and near linear potential profile in **0 cm BPE** case, Figure 3c. Consequently, as shown in Figure 3d, two major features in the |∇φ| *vs.* x plots can be observed, one present near the edge of BPE and the second one in close proximity to the surface of the feeder electrode. The insert in Figure 3d shows that, the latter feature is also observed in **0 cm BPE** model samples. As the BPE length is increased, these two features merge as the BPE and FE become closer to one another resulting in higher absolute field strengths in this increasingly narrow gap, Figures S4a and b. These features in the |∇φ| *vs.* x plots can be further investigated by analyzing the vector components of the potential gradient. When no BPE is present (Figure S4c) only the negative values in the x-direction contribute to the overall gradient being a consequence of the relatively homogeneous distribution of the current flow except the edges of FEs. In the exemplary case of the **1.4 cm BPE** model sample (Figure S4d), the significantly conducting surface of FTO becomes the major current pathway resulting in inhomogeneous current distribution within an overall system, especially at the corners of BPE. Therefore, the dominant contribution in the x-direction with a negative gradient exhibits two features in |∇φ| *vs.* x plots governed by the distance between BPE and FE edges. This predicted behavior closely mirrors the experimental observations shown in Figure 2a, *i.e.*, enhanced PEDOT deposition close to the edges of the BPE. At the BPE edges, both positive and negative gradients in the z-direction are found with ϕ_z minimum at BPE surface in anodic ($\varphi < 0$) and ϕ_z maximum in cathodic ($\varphi > 0$) regions of BPE. However, the specific pattern in |∇φ| is clearly dominated by electric field vectors pointing in the x-direction. Consequently, the equipotential BPE surface imposes increasingly positive solution overpotentials ($\varphi_{BPE} - \varphi > 0$) in the anodic region as the distance in the z-direction from BPE increases.

In order to quantify the effect of the inclusion of BPE on the whole FTO/medium interfacial area, |∇φ| *vs.* x plots for all the studied systems were subjected to integration. The resulting potential values were plotted against the total applied voltage divided by two, Figure 4a. For the **0 cm BPE** model sample, the calculated slopes of the fitting lines are close to unity representing relatively high homogeneity in the electric field distribution. In the case of BPE model samples, higher than unity slopes were obtained (**1.4 cm BPE** = 1.30, **2 cm BPE** = 1.52, and **2.6 cm BPE** = 1.89). The increase as the BPE is moved closer to the feeder electrode arises from decreasing homogeneity in the electric field distribution in the system. Figure 4b shows the

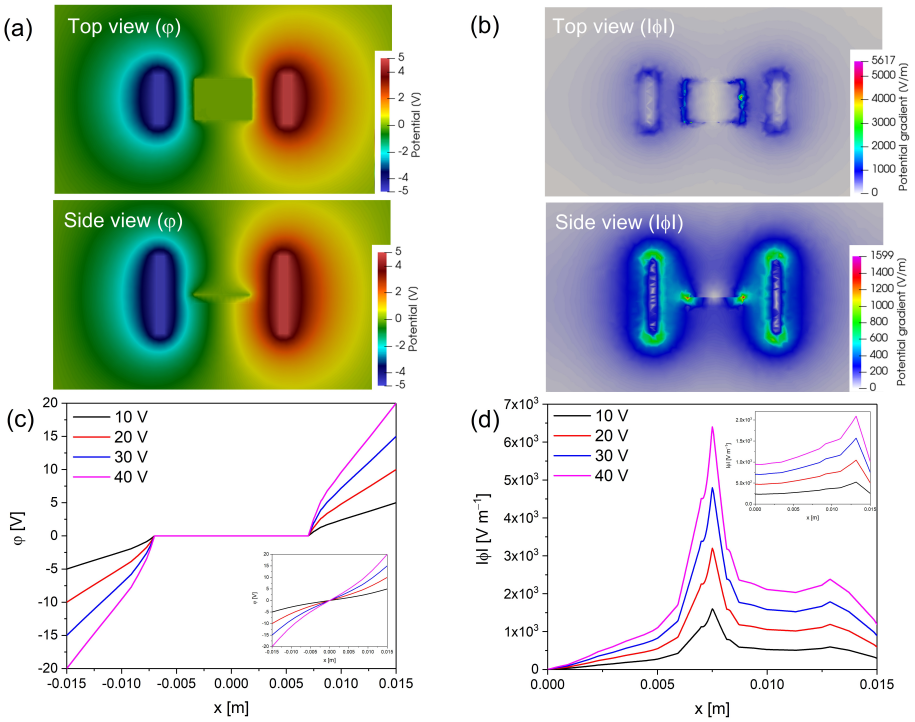

Figure 3. Exemplary φ (a) and |∇φ| (b) distribution maps for 1.4 cm BPE, together with cross-sectional profiles for φ (c) and |∇φ| (d) at the center and surface of BPE for different applied potentials. Inserts: corresponding φ (c) and |∇φ| (d) profiles taken in the absence of BPE.

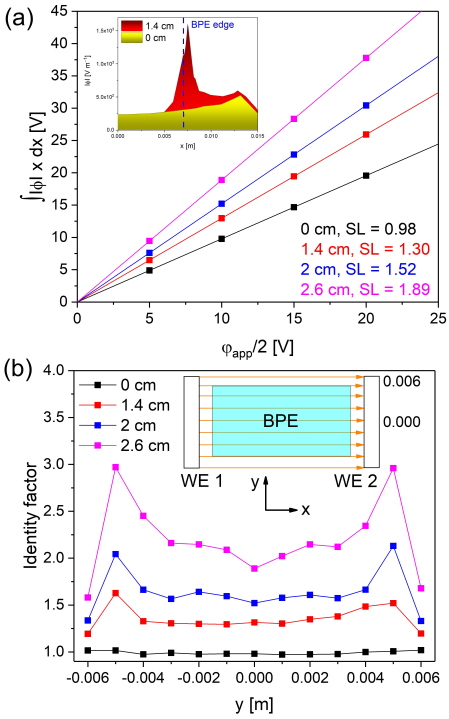

Figure 4. Integrated areas under |ϕ| vs. x curves (from BPE or cell center to WE) as a function of half of the applied potential to calculate the slope (SL) of the fitting lines (a). SL distribution for all studied samples at 0.001 m intervals covering BPE and edges of WEs (b). Inserts: visual comparison of integrated areas between 1.4 cm BPE and 0 cm BPE samples (a), and schematic representation of BPE system geometry (b).

global distribution of slopes. For all BPE model samples, the lowest slopes are observed at the center of the long axis of the BPE (0.000 m) and peak at the BPE edges (±0.005 m). At 0.1 cm beyond BPE edges the drop in slope is substantial, but it does not become unity, suggesting a significant enhancement in the electric field strength at relatively large distances (from a diffusion perspective) away from the long BPE edges.

Figure 5a shows plots of |ϕ| *vs.* distance/location on the BPE (x = center→edge, y = ±0.005 m) and demonstrates the significant effect of the BPE edges on the local field strength. Specifically, there is approximately a two-fold increase in |ϕ| at the long BPE edges even as the BPE length is increased from 2 to 2.6 cm. In all cases, the |ϕ| distribution exhibits slight irregular features in proximity to the central axis. Previous FEM investigations[35,36] on inhomogeneous dielectric interfaces have shown that various surface defects can have notable effect on local electric fields. Different mesh sizes were tested for the **1.4 cm BPE** model sample and demonstrated the importance of having a sufficiently fine mesh to avoid mesh-related artifacts. To quantify the rate of change of the electric field strength with position, single exponential decays were fitted to the |ϕ| *vs.* x profiles to give a distance-dependent field strength decay factor that could be conveniently compared for different BPE lengths and feeder voltages. The following equation was used:

$$f(x) = Aexp(Bx) \tag{3}$$

where, A is |ϕ| value at the BPE center (in V m^{-1}) and B is the rate factor (in m^{-1}). Exemplary fitting ($\triangle\varphi_{app}$ = 10 V, y = 0.000 m) to Equation 3 is presented in Figure S5. Rate factors, B, of 595,

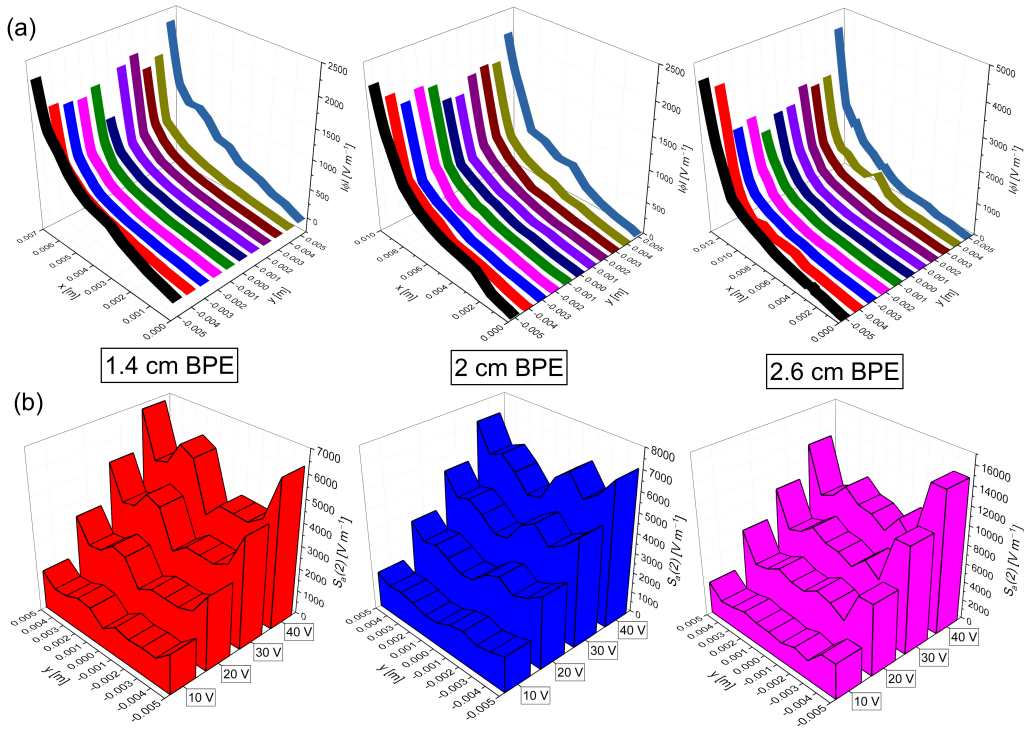

Figure 5. Exemplary |ϕ| distribution plots ($\Delta\varphi_{app}$ = 10 V) at BPE surfaces in x and y directions (a). Field strength distributions on BPE surfaces (± y) at different applied potentials obtained from integration of Equation 4 (b).

415, and 480 m^{-1} were obtained for the 1.4, 2, and 2.6 cm long BPEs, respectively. The obtained rates are independent of applied voltage and likely reflect the "mid-range" position of **2 cm BPE** among studied model samples in terms of its effect on φ and Iϕl distributions. To obtain "smooth" datasets of the global distribution of field strengths, firstly, the calculated A and B values were used to construct the following derivative of Equation 3 for all considered systems:

$$f'(x) = ABexp(Bx) \quad (4)$$

where, AB is the initial value of the rate of change (in V m^{-2}). Representative distribution plots according to Equation 4 can be seen in Figure S6b. Secondly, all of the BPE systems expressed with Equation 4 were integrated with respect to x-direction (*vide* insert in Figure 4b) to construct voltage-dependent distribution plots of field strength, Figure 5b. Notably, the resultant distribution patterns are visually consistent with actual PEDOT/FTO samples (Figure 2a), thus predicting enhanced PEDOT deposition at BPE edges and corners due to enhanced electric field strengths and hence a greater driving force for EDOT oxidation.

The theoretical limitation of the linear model discussed earlier when no electrolyte is present, as well as relatively small calculated solution potential values in close proximity to the BPE surface (*vide* Figure S3), indicated a need for alternative explanations of the obtained non-linearities in PEDOT deposition patterns. We therefore speculate that homogeneous reactions driven by the significant potential difference between the BPE and solution, along with subsequent diffusive mass transport of the products play a dominant role. To determine the region where the potential is sufficient to oxidize EDOT in the vicinity of the BPE, both φ and Iϕl values were calculated for different heights above the BPE for distances, △z, up to $1x10^{-3}$ m and the results obtained are shown in Figures 6a and b. The potential range values increase significantly (approximately proportionally) with increasing distance in the direction perpendicular to the BPE surface, while Iϕl profiles and their ranges of magnitude remain the same up to $\triangle z = 1x10^{-4}$ m. Predictably, φ maximizes at the BPE edges, with the highest values being observed for the **2.6 cm BPE** followed by **2 cm BPE** and **1.4 cm BPE** model samples. As can be seen from Figure 5c, the vector field lines are evenly distributed along the BPE surface with the most intensity in proximity to the BPE edge (*vide* overlaid color map). Since $\vec{J} = \sigma\vec{E}$, the presented field lines reflect all possible current pathways in the system. Due to the significant difference between the electrical conductivity of the FTO layer and medium (~10^{10} ratio), the majority of the current passes through the FTO layer. On the other hand, notable current flow occurs in solution at the corners/edges and through the edge facing the feeder electrode.

In the simplified oxidative PEDOT polymerization process, the initiation reaction is a radical cation formation (EDOT→ $EDOT^{+\bullet}$) followed by radical-radical coupling ($EDOT^{+\bullet}$ + $EDOT^{+\bullet}$→2EDOT). The polymerization continues with the oxidation of dimer/oligomers occurring at successively lower oxidation potential, *i.e.*, the effective driving force increases as polymerization proceeds. At a certain chain length, the product

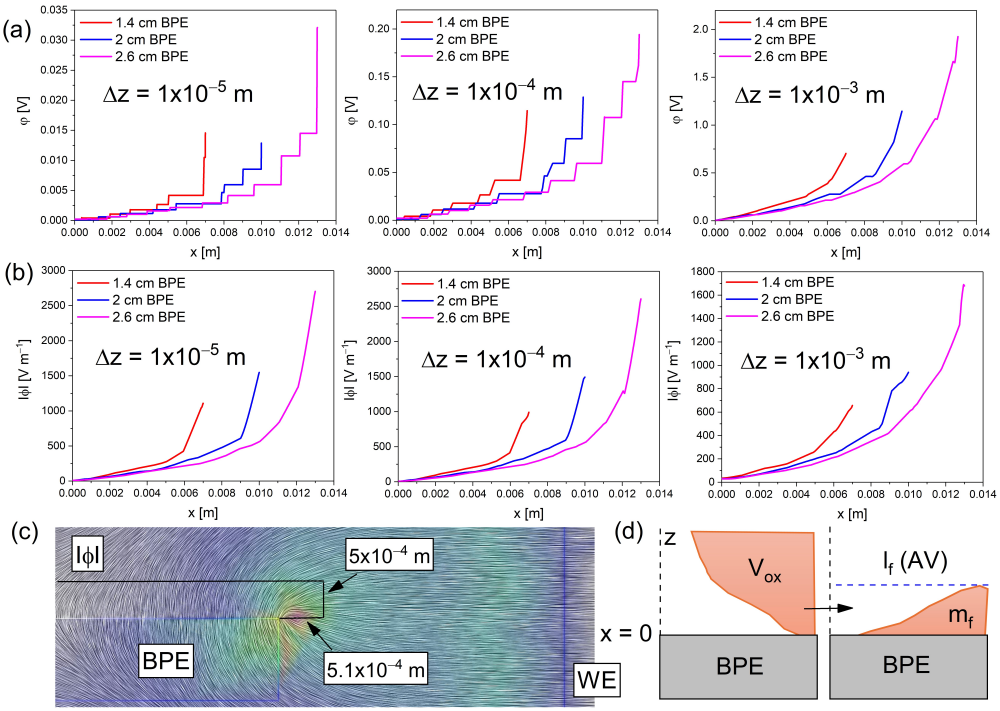

Figure 6. Representative φ (a) and Iϕl (b) profiles ($\Delta\varphi_{app} = 10$ V) at the center of BPE for three different distances along the z-axis (△z). Potential gradient map of studied systems with indicated vector field lines and unscaled marking (black lines) of the region near BPE considered in mass transport of EDOT entities (c). Schematic representation of the hypothetical volume of oxidized EDOT (V_{ox}) above BPE, together with the profile of deposited film with marked average film thickness (l_f) and total mass (m_f) characteristics (d).

becomes insoluble in the medium and thus deposits on the electrode surface. Due to the significant complexity of the electrochemical polymerization of conducting polymers, at this stage of research, we consider only the initial steps, as well as exclude dynamic changes in solution conductivities originating from generated and/or reacted hydronium ions. Independent experiments in a conventional 3-electrode system indicate that the oxidation potential of EDOT is approximately 0.8 V.[37] Therefore, this value was set as a threshold limit to estimate the fraction of oxidized EDOT molecules within the relevant vicinity of BPE. Firstly, the maximum thickness of the layer of solution in which 2EDOT can be oxidized within the experimental time is calculated assuming diffusion control. The diffusion coefficient (D) for 2EDOT was estimated to be approximately $4.34x10^{-10}$ $m^2 s^{-1}$. The diffusion length (l_D) was calculated using $l_D \approx \sqrt{Dt}$. For a deposition time, t, of 10 min, l_D is $5.1x10^{-4}$ m. Therefore, the considered volume of the medium above BPE and the hypothetical 'volume' of oxidized EDOT (V_{ox}) were limited by $5.1x10^{-4}$ m in the x-direction and $5x10^{-4}$ m in the z-direction, Figure 6c. The latter limitation was selected to accommodate six vertical intervals for calculations of (△x)(z) surface areas (*vide* Figure S7a). Herein, the △x notation represents a fraction of oxidized EDOT along the x-axis above 0.8 V in φ *vs.* x plots. For each vertical interval, two fractions were considered totaling △x: at the plane of BPE ($\triangle x_1$) and beyond the BPE edge ($\triangle x_2$). For V_{ox} calculations two integrations were conducted along the x, y, and z dimensions, Figures S7 and S8. Resultant V_{ox} values were used to estimate the average film thickness (l_f) and mass of deposited film (m_f), Figures 7a and b. The analysis of the plots used for the first integration step in V_{ox} estimations reveals an interesting rationale for the non-linear deposition profile (*vide* Figure 2b) obtained for the **1.4 cm BPE** samples. As can be seen from Figure S7b, at $\triangle\varphi_{app} =$ 10 V the oxidized fraction of EDOT expressed as $\triangle x = \triangle x_1 + \triangle x_2$, is only above zero for y = 0.003, 0.004, and 0.005 m. Moreover, in those cases, the $\triangle x_2$ contribution is significant in sharp contrast to **2 cm BPE** and **2.6 cm BPE** model samples, Figures S7 c and d. For **1.4 cm BPE**, non-zero △x fractions for all y values are only obtained when $\triangle\varphi_{app} \geq 20$ V.

Importantly, the calculated V_{ox} values can be used for both m_f and l_f estimations, Figure 6d. All of the resultant m_f *vs.* $\triangle\varphi_{app}$ plots (*vide* Figure 7a) are linear, displaying increasing slope values with increasing lengths of BPE (**1.4 cm BPE** = $2.33x10^{-7}$ g V^{-1}, **2 cm BPE** = $3.17x10^{-7}$ g V^{-1}, and **2.6 cm BPE** = $5.26x10^{-7}$ g V^{-1}). The corresponding l_f *vs.* $\triangle\varphi_{app}$ plots can be constructed assuming a PEDOT film density of 1 g cm^{-3}, Figure 7b. The obtained slope values (**1.4 cm BPE** = $3.32x10^{-9}$ m V^{-1}, **2 cm BPE** = $3.17x10^{-9}$ m V^{-1}, and **2.6 cm BPE** = $4.05x10^{-9}$ m V^{-1}) indicate the proximity of average l_f values for **1.4 cm BPE** and **2 cm BPE** model samples. The average l_f value obtained for a **2 cm BPE** sample electrodeposited at $\triangle\varphi_{app}$ = 30 V and 20 min is around $1.54x10^{-7}$ m, Figure S9. Significantly, this value is very close to the calculated l_f for **2 cm BPE** (*i.e.* $1.53x10^{-7}$ m) based on $3.17x10^{-9}$ m V^{-1} slope and considered deposition time.

When assuming the theoretical specific charge of EDOT to be 679 C g^{-1} (for single electron transfer), film mass can be converted to the charge stored in the film (Q_V), Figure 7c. The obtained Q_V values were used for the calculation of hypo-

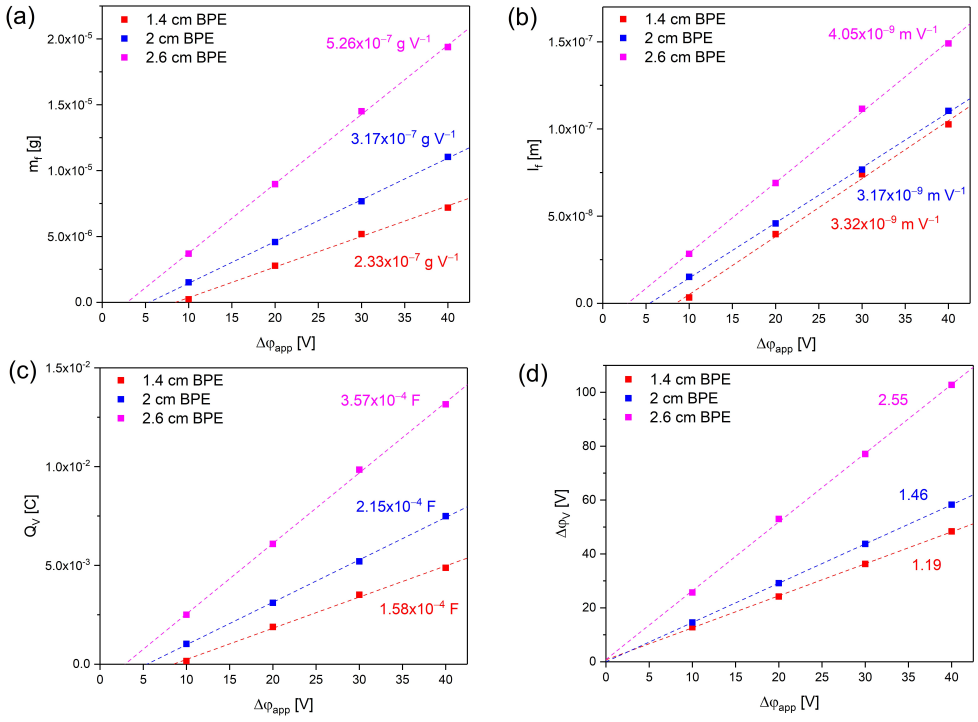

Figure 7. Calculated change in film mass based on V_{ox} (a) and corresponding average film thickness (b) as a function of applied potential, together with marked SL values. Hypothetical charge (Q_V) values based on calculated total V_{ox} (c) and conceptual "volumetric voltage" (△φV) obtained from integration of plots in Figure 5b (d) as a function of applied potential, together with marked SL values.

thetical film capacitances for studied BPE systems. The corresponding voltage ($\triangle\varphi_V$) values were found from the integration of the results presented in Figure 5b with respect to the y-axis. The resultant $\triangle\varphi_V$ *vs.* $\triangle\varphi_{app}$ plots (*vide* Figure 7d) exhibit the same trends as m_f and thus Q_V plots. As can be seen from Figures 7c and d, the slope values in both cases are indeed closely proportional. The exact physical interpretation of $\triangle\varphi_V$ is an open question. This quantity is based on the consideration of potential gradient distribution at the BPE/medium interface, while film mass and charge quantities include consideration of potential distribution at both the interface and the electrode vicinity limited by diffusion. It can be speculated that $\triangle\varphi_V$ represents the area-dependent voltage at the BPE surface exerted by an electric field controlled by the specific geometry of the BPE system. The calculated $Q_V/\triangle\varphi_V$ ratios representing hypothetical C_f values as a function of applied voltages are shown in Figure 8. The resultant profiles for all studied BPE systems are in good agreement with deposition profiles obtained *via* electrochemical measurements (*vide* Figure 6d). The non-linear profile for the **1.4 cm BPE** sample is reproduced, as well as, to a notable extent the intertwined profiles for the **2 cm BPE** and **2.6 BPE** samples. Moreover, the model-derived film capacitance profiles are also similar to calculated admittance profiles that are related to diffusivity in the PEDOT films, Figure 2c.

Due to the expected very large Debye lengths at BPE/medium interfaces in high-resistance solutions, the nature of BPE reactions deserves attention. *i.e.*, because of the low ion concentration, the Debye length may exceed the distance over which it is reasonable to expect heterogeneous electron transfer. On the other hand, the reactions at titanium FEs are rather straightforward to identify. At the positively charged FE, the growing TiO_2 layer occurs driven by a tandem of two anodic reactions: (i) $Ti^0 \rightarrow Ti^{4+} + 4\bar{e}$ and (ii) $Ti^{4+} + 2H_2O \rightarrow TiO_2 + 4H^+$.[38] Freshly polished titanium surfaces readily oxidize at ambient conditions forming *ca.* 1.5 nm thick layers, and further anodic oxidation results in significant TiO_2 growth in the order of tens of nm.[39] At negatively charged FE cathodic reduction of TiO_2 at acidic conditions proceeds as follows, $TiO_2 + 4H^+ + \bar{e} \rightarrow Ti^{3+}{}_{(aq)} + H_2O$.[40] Listed here titanium FE reactions are confirmed by consecutive observations and are important determinants for dielectric properties of the medium in studied systems, yet their temporal evolution does not affect effective FE potentials nor electric field distribution in the vicinity of BPE. As can be seen from Figure S10a, anodic passivation of Ti FEs in both monomer-free and EDOT ultrapure water solutions during bipolar experiments is apparent. The oxidation of the monomer and subsequent PEDOT film formation is impeded by TiO_2 layer development. The estimated pH values before and after PEDOT deposition on BPEs are *ca.* 6, which implies a preference for cathodic reduction of TiO_2 to Ti^{3+} cations at negative FE. Based on utilized FE dimensions the estimated complete TiO_2 layer disintegration with a hypothetical thickness of 1.5 nm would result in only ~$1.2x10^{-5}$ M extra titanium ions that could contribute to overall ionic strength. Control studies of PEDOT deposition at BPEs in a series of increasing electrolyte content from 10^{-9} to 10^{-1} M $NaClO_4$ reveal that from 10^{-3} M, severe corrosion at anodic FE occurs (*vide* Figure S10b) accompanied by hydrogen gas generation at both cathodic FE and cathodic extremity of BPE. As a result, overoxidized PEDOT films are formed at the anodic part of BPEs even at relatively low applied potentials, Figure S10c. Notably, no gas evolution was observed at any electrode surface during experiments presented in Figure 2a, as well as control experiments with $NaClO_4$ concentrations from 10^{-9} to 10^{-4} M.

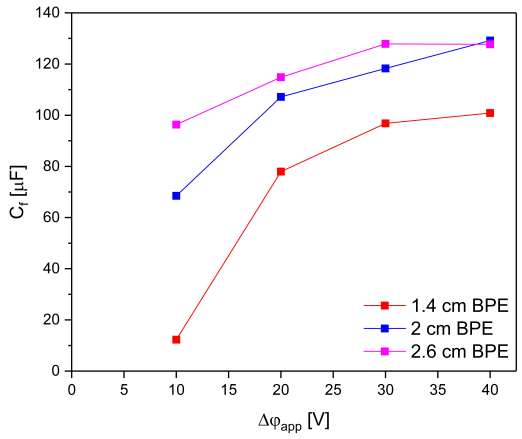

Figure 8. Hypothetical film capacitance (C_f) values based on $Q_V/(\Delta\varphi_V)$ ratios.

FEs taking part in bipolar experiments (10 mM EDOT in ultrapure water solutions) with **2 cm BPE** samples exposed to 30 V for 40 min were subjected to EIS measurements to estimate the specific capacitance of deposited PEDOT film, Figure S10d. The obtained value of *ca.* 0.6 mF cm^{-2} constitutes only 10% of all PEDOT deposited since concurrent PEDOT film on BPE in this system exhibits around 5 mF cm^{-2} capacitance. Therefore, indeed anodic passivation of positive FE significantly inhibits PEDOT film formation on itself. Anodic oxidation of EDOT on both positively charged FE and BPE surface starts with the following reactions: (i) $EDOT \rightarrow EDOT^{+\bullet} + \bar{e}$ and (ii) $EDOT^{+\bullet} + EDOT^{+\bullet} \rightarrow 2EDOT + 2H^+$ *etc.* When the growing polymer chain attains a certain length it loses solubility and deposits on the electrode surface. Generated protons from dimerization steps and already mentioned titanium ions from the cathodic reduction of the oxide layer on negative FE contribute to specific ionic characteristics of the bipolar electrochemical system. In order to gain insight into apparent electrolytic characteristics we measured the solution conductivities at different polymerization times from 5 to 40 min for **2 cm BPE** samples in ultrapure water exposed to 30 V with and without 10 mM EDOT, Figure S11. Recorded solution conductivity values for different concentrations of EDOT in ultrapure water samples are significant (*vide* Figure S11a), arriving at the value of *ca.* 8 μS cm^{-1} for 10 mM concentration. As can be seen from Figure S11b, which presents conductivity sensor calibration, the maximal EDOT concentration in our systems roughly corresponds to 10^{-4} M equivalent of KCl in terms of conductivity.

Interestingly, it was observed that polymerization solution conductivities decreases as electrodeposition proceeds which is

in sharp contrast to the control study where the conductivity increases when the BPE is polarized in monomer-free ultrapure water samples, Figure S11c. It can be speculated that in the case of monomer-free samples, a slight and non-linear increase in conductivity is predominantly related to a cathodic reduction of the oxide layer at negative FE since the previously estimated value of $1.2x10^{-5}$ M titanium ions roughly matches the "concentration-conductivity" region of interest. Importantly, despite proton generation at each dimerization step, there is a clear linear decrease in conductivity with polymerization time likely reflecting PEDOT formation kinetics. Results presented in Figure S11 suggest that the studied bipolar electrochemical systems in this work are within the 10^{-5} to 10^{-4} M range, leading to very large Debye lengths between 90 to 30 nm. The electron tunneling probability through the distance of ~1 nm of the water layer yielding a 2 eV energy barrier is empirically estimated[41] to be around $6x10^{-6}$ and consistent with the Gamov tunneling equation.

Oxidation of EDOT *via* heterogeneous electron transfer at BPE surfaces is evident at 10^{-3} M concentrations of supporting electrolyte, in studies before[17,18] and also in this work. Therefore, a significantly large interfacial potential difference is created in close proximity to the Stern layer already at this concentration level. We did not include charging conditions at electrode boundaries in the FEM modeling but estimated the hypothetical maximum polarization voltage ($\triangle\varphi_{BPE}$) based on the calculation of potential at BPE extremities induced by increasing the conductivity of the medium. Those FEM simulations were conducted on **1.4 cm BPE** model sample with medium conductivity values equivalent to KCl in the 10^{-5} to 10^{-1} M range with $\triangle\varphi_{app} = 10$, 20, and 40 V, Figure 9. It is conspicuous that within the 10^{-3} to 10^{-1} M range the induced polarization of ~10 to 360 mV at *e.g.* $\triangle\varphi_{app} = 40$ V is enough to drive EDOT oxidation *via* heterogeneous electron transfer if the effective capacitance of electric double layer and thus the local surface charge of BPE are considered. On the other hand, estimated 10 and 20-fold lower polarization potential values at 10^{-5} and 10^{-4} M (in reference to polarization induced at 10^{-3} M) suggest very low probability for electron tunneling, *e.g.*, using 2 eV energy barrier.

Thus, in pure milli-Q water one would not expect significant heterogeneous electron transfer to be possible based on the Debye length and the voltage induced in the BPE, but a relatively small increase in solution concentration, *e.g.*, arising for protons released during EDOT oxidation or dissolution or titanium oxide at the feeder cathode. It appears that there is significant scope for further investigations into electron transfer dynamics when the electric double layer is underdeveloped using wirefree methods that avoid iR drop effects, as well as including scanning probe methods to measure the potential drop when approaching the BPE surface.

Overall, the presented theoretical framework qualitatively replicates observed non-linearities in film capacitance profiles for the wirefree deposition of conducting polymers. The successful prediction of deposition patterns for a highly complex process of conducting polymer film formation constitutes an important first step toward understanding bipolar electrochemistry in high-resistance solutions. Significantly, the modeled non-linear change in solution overpotentials imposed by the equipotential surface of BPE combined with calculated relatively low electric field strengths (<6 kV m^{-1}) in close proximity to the BPE-solution interface indicates that PEDOT electrosynthesis is likely to involve homogeneous electron transfer where the double layer is not well developed. In the future, we plan to build a model that accounts for the influence of growing PEDOT film layers on the physicochemistry of the BPE-solution interface as well as radical cation transport and acceleration due to the presence of the interfacial and feeder-driven electric fields. Additionally, since a well-developed electrical double layer is needed to screen the charge resulting from BPE polarization induced by an electric field, new theoretical considerations (aided with quantum and molecular dynamics simulations) are needed to model various interfacial electric field effects at suboptimal ion concentrations.

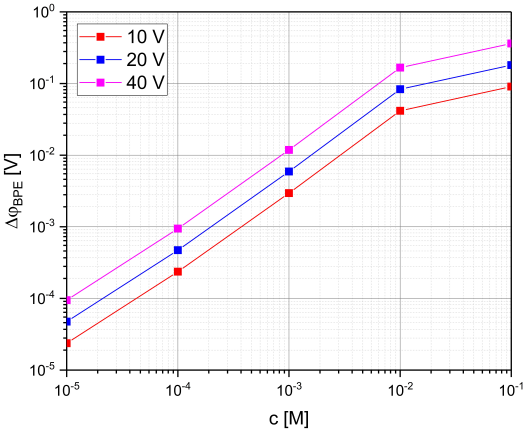

Figure 9. Hypothetical maximum polarization voltage of the exemplary 1.4 cm BPE ($\Delta\varphi_{BPE}$) calculated for different medium conductivities equivalent to KCl concentrations in the 10^{-5}–10^{-1} M range.

Conclusions

We have successfully fabricated electrically conducting polymer PEDOT films in ultrapure water utilizing bipolar electrochemistry. Such deposition would not be possible in "traditional" 3-electrode systems where the presence of a supporting electrolyte is needed. We demonstrated that the PEDOT deposition profiles cannot be fully explained by commonly assumed linear decay of the electric field through the solution driven by the feeder voltages. Our FEM model provides a rationale for the observed preferential deposition areas and provides deep insights into mass transport and quantifies the volume of solution above the BPE that could be available for deposition. Importantly, we have been able to calculate both the hypothetic film charge and BPE voltage that depends markedly on the physical location on the BPE. Taken together, this model successfully replicates the film capacitance profiles of studied

PEDOT-BPE systems obtained experimentally. The proposed alternative framework provides a valuable starting point for understanding the electrochemical deposition process on BPEs in high-resistance media. We envision further investigations where polymer layers are modeled to target various charge transfer and polarization effects on hetero- and homogeneous reactions in dynamic bipolar systems with low ion content.

Supporting Information

The following auxiliary details can be found in the Supporting Information document: electrochemical characterization of PEDOT films deposited on BPEs, film capacitance values of studied PEDOT-BPE systems *via* CV and EIS, exemplary potential and potential gradient maps of studied BPE systems, plots of various potential and potential gradient profiles in BPE systems, exemplary fittings to exponential decay function for |ϕ| *vs.* x plots, selected global potential gradient distributions at BPE-solution interface, schematics and plots for diffusive mass transport calculations, exemplary PEDOT film thickness estimation deposited on BPE, data regarding feeder and bipolar electrode reactions, and polymerization solutions conductivity assessment.

Acknowledgements

This publication has emanated from research supported in part by a research grant from Science Foundation Ireland (SFI) under Grant Number 21/RC/10294_P2 and co-funded under the European Regional Development Fund and by FutureNeuro industry partners. The support of Science Foundation Ireland under the SFI US-Ireland R&D Partnership Programme Proposal ID: 21/US–C2C/3768 is deeply appreciated. This work has received funding under the European Union's MSCA Doctoral network "ECLectic", Horizon Europe programme Grant Agreement Number 101119951.

Conflict of Interests

The authors declare no conflict of interest.

Data Availability Statement

The data that support the findings of this study are available from corresponding authors upon reasonable request.

Keywords: Bipolar electrochemistry · Polymers · Deposition · Finite element method · Electron transfer

[1] P. Sanjuan-Alberte, M. R. Alexander, R. J. M. Hague, F. J. Rawson, *Bioelectron Med* **2018**, *4*, 1–7.
[2] M. R. Love, S. Palee, S. C. Chattipakorn, N. Chattipakorn, *J. Cell. Physiol.* **2018**, *233*, 1860–1876.
[3] M. R. Cho, H. S. Thatte, M. T. Silvia, D. E. Golan, *The FASEB Journal* **1999**, *13*, 677–683.
[4] R. J. Forster, *Curr. Opin. Electrochem.* **2023**, *39*, 101297.
[5] S. E. Fosdick, K. N. Knust, K. Scida, R. M. Crooks, *Angew. Chem. Int. Ed.* **2013**, *52*, 10438–10456.
[6] C. Qin, Z. Yue, Y. Chao, R. J. Forster, F. Maolmhuaidh, X. F. Huang, S. Beirne, G. G. Wallace, J. Chen, *Appl Mater Today* **2020**, *21*, 100804.
[7] C. Qin, Z. Yue, X. F. Huang, R. J. Forster, G. G. Wallace, J. Chen, *Appl Mater Today* **2022**, *27*, 101481.
[8] B. Guo, P. X. Ma, *Biomacromolecules* **2018**, *19*, 1764–1782.
[9] R. Balint, N. J. Cassidy, S. H. Cartmell, *Acta Biomater.* **2014**, *10*, 2341–2353.
[10] K. Duval, H. Grover, L. H. Han, Y. Mou, A. F. Pegoraro, J. Fredberg, Z. Chen, *Physiology* **2017**, *32*, 266–277.
[11] F. Mavré, K. F. Chow, E. Sheridan, B. Y. Chang, J. A. Crooks, R. M. Crooks, *Anal. Chem.* **2009**, *81*, 6218–6225.
[12] Y. Ishiguro, S. Inagi, T. Fuchigami, *J. Am. Chem. Soc.* **2012**, *134*, 4034–4036.
[13] Y. Koizumi, N. Shida, M. Ohira, H. Nishiyama, I. Tomita, S. Inagi, *Nat. Commun.* **2016**, *7*, DOI 10.1038/ncomms10404.
[14] J. Lee, T. W. Yoon, S. Chung, K. Cho, G. Zhang, B. Kang, *Adv. Funct. Mater.* **2024**, DOI 10.1002/adfm.202406229.
[15] J. F. L. Duval, G. K. Huijs, W. F. Threels, J. Lyklema, H. P. Van Leeuwen, *J. Colloid Interface Sci.* **2003**, *260*, 95–106.
[16] J. F. L. Duval, *J. Colloid Interface Sci.* **2004**, *269*, 211–223.
[17] A. Eden, K. Scida, N. Arroyo-Currás, J. C. T. Eijkel, C. D. Meinhart, S. Pennathur, *J. Phys. Chem. C* **2019**, *123*, 5353–5364.
[18] A. Eden, K. Scida, N. Arroyo-Currás, J. C. T. Eijkel, C. D. Meinhart, S. Pennathur, *Electrochim. Acta* **2020**, *330*, 135275.
[19] A. N. Colli, H. H. Girault, *J. Electrochem. Soc.* **2017**, *164*, E3465–E3472.
[20] T. Nann, J. Heinze, *Electrochem. Commun.* **1999**, *1*, 289–294.
[21] C. Ulrich, O. Andersson, L. Nyholm, F. Björefors, *Anal. Chem.* **2009**, *81*, 453–459.
[22] N. Pébère, V. Vivier, *ChemElectroChem* **2016**, *3*, 415–421.
[23] J. Song, *FEBS Lett.* **2009**, *583*, 953–959.
[24] A. Dér, L. Kelemen, L. Fábián, S. G. Taneva, E. Fodor, T. Páli, A. Cupane, M. G. Cacace, J. J. Ramsden, *J. Phys. Chem. B* **2007**, *111*, 5344–5350.
[25] K. B. Oldham, *J. Electroanal. Chem.* **2008**, *613*, 131–138.
[26] G. Meaden, in *Electrical Resistance of Metals*, Springer, Boston, MA, **1965**.
[27] *Handbook of Chemistry and Physics*, CRC Press, **1997**.
[28] M. Malinen, P. Råback, in *Elmer Finite Element Solver for Multiphysics and Multiscale Problems, Multiscale Modelling Methods for Applications in Material Science* (Eds.: I. Kondov, G. Sutmann), **2013**, pp. 101–113.
[29] E. Villani, S. Inagi, *Anal. Chem.* **2021**, *93*, 8152–8160.
[30] K. Scida, A. Eden, N. Arroyo-Currás, S. Mackenzie, Y. Satik, C. D. Meinhart, J. C. T. Eijkel, S. Pennathur, *ACS Appl. Mater. Interfaces* **2019**, *11*, 13777–13786.
[31] B. A. Boukamp, *Solid State Ion* **1986**, *20*, 31–44.
[32] A. Bonnefont, F. Argoul, M. Z. Bazant, *J. Electroanal. Chem.* **2001**, *500*, 52–61.
[33] E. M. Itskovich, A. A. Kornyshev, M. A. Vorotyntsev, *Physica A* **1977**, *39*, 229–238.
[34] M. Van Soestbergen, *Russ. J. Electrochem.* **2012**, *48*, 570–579.
[35] S. M. Risser, K. F. Ferris, *Mater. Lett.* **1992**, *14*, 99–102.
[36] K. F. Ferris, S. M. Risser, *Chem. Phys. Lett.* **1995**, *234*, 359–366.
[37] L. Pigani, A. Heras, Á. Colina, R. Seeber, J. López-Palacios, *Electrochem. Commun.* **2004**, *6*, 1192–1198.
[38] M. Brocklebank, H. Feltham, J. J. Noël, L. V. Goncharova, *Electrochim. Acta* **2022**, *435*, 141342.
[39] D. Prando, A. Brenna, M. V. Diamanti, S. Beretta, F. Bolzoni, M. Ormellese, M. P. Pedeferri, *J Appl Biomater Funct Mater* **2018**, *16*, 3–13.
[40] T. Ohtsuka, M. Masuda, N. Sato, *J. Electrochem. Soc.* **1987**, *134*, 2406–2410.
[41] W. Schmickler, *Surf. Sci.* **1995**, *335*, 416–421.

Manuscript received: August 19, 2024
Revised manuscript received: December 12, 2024
Version of record online: February 17, 2025